INSTITUTE OF PHYSICS PUBLISHING MODELLING AND SIMULATION IN MATERIALS SCIENCE AND ENGINEERING

Modelling Simul. Mater. Sci. Eng. **10** (2002) 1–19 PII: S0965-0393(02)55385-7

Accuracy and convergence of parametric dislocation dynamics

Jianming Huang and Nasr M Ghoniem[1]

Mechanical and Aerospace Engineering Department, University of California, Los Angeles, CA90095-1597, USA

E-mail: ghoniem@ucla.edu

Received 28 July 2002, in final form 22 October 2002
Published
Online at stacks.iop.org/MSMSE/10

Abstract

In the parametric dislocation dynamics (PDD), closed dislocation loops are described as an assembly of segments, each represented by a parametric space curve. Their equations of motion are derived from an energy variational principle, thus allowing large-scale computer simulations of plastic deformation. We investigate here the limits of temporal and spatial resolution of strong dislocation interactions. The method is demonstrated to be highly accurate, with unconditional spatial convergence that is limited to distances of the order of interatomic dimensions. It is shown that stability of dislocation line shape evolution requires very short time steps for explicit integration schemes, or can be unconditionally stable for implicit time integration schemes. Limitations of the method in resolving strong dislocation interactions are established for the following mechanisms: dislocation generation, annihilation, dipole and junction formation, pileup evolution.

1. Introduction

Since it was first introduced in the mid-eighties [1, 2], dislocation dynamics (DD) has now become an attractive tool for investigations of both fundamental and collective processes that constitute plastic deformation of crystalline materials. In its early versions, the collective behaviour of dislocation ensembles was determined by direct numerical simulations of the interactions between infinitely long, straight dislocations. The numerical accuracy and limitations of the two-dimensional description of dislocation ensemble evolution has been examined in considerable detail (e.g. [3–11]). Although the numerical issues of stability, accuracy, convergence and field approximations have been largely resolved in the two-dimensional case, it has been realized that the fundamental physical nature of dislocation

[1] Author to whom correspondence should be addressed.

loops, being three-dimensional space curves, makes progress with rigorous two-dimensional simulations rather difficult without additional *ad hoc* rules of close-range interactions. Such realization prompted several research groups to consider extensions of the DD methodology to the more physical, yet, considerably more complex conditions of three-dimensional DD computer simulations of plastic deformation. Developed methods for three-dimensional DD can be categorized into two groups, according to the line discretization scheme. The first group uses straight segments: either pure edge or screw [12–21], or segments of mixed character [22, 23]. The second category is based on curved segments; the so-called parametric method [30–33].

There is an enormous range of problems related to spatial resolution of plasticity, spanning from nano-, micro-, and single crystal materials, all the way up to polycrystalline material deformation. In addition, many physical mechanisms involving dislocations are inherently either stable or unstable. For example, when an external stress is applied to a Frank–Read (FR) source, the dislocation develops an equilibrium shape at low values of applied stress. However, above a critical or *threshold* stress, the dislocation line becomes unstable, and may expand significantly without additional increments of applied stress. Most dislocation reactions have this *dynamic* feature, where junctions, dipoles, pileups, can all be either stable or unstable, depending on some critical stress level. It is therefore important to develop an understanding of the numerical accuracy, convergence and stability, so that one can actually resolve such critical reactions without the doubt that the results are numerical artefacts. We plan to provide an exposition of the numerical features of parametric dislocation dynamics (PDD) method, when applied to the most significant dislocation interaction problems. We limit ourselves to the numerical features of the PDD, since discretization methods based on straight segments have other features of resolution that are outside the scope of the current investigation.

The PDD methodology is based on two main principles that are often employed in modern numerical methods of continuum mechanics (i.e. the finite element method (FEM)). The first is some energy-based variational principle that would allow one to derive the equations of motion (EOM) of a *reduced set* of degrees of freedom (DOF) representing the system. The second principle is a *kinematic* assumption regarding how the displacement or strain field is assumed to vary in a specified region of the continuum. To draw the analogy, a minimization of the Gibbs free energy of a single loop upon its virtual motion in the external and internal field results in the EOM, while assumed spline functions between some fixed nodes on the dislocation loop corresponds to the kinematic assumption of continuum mechanics. The variational principle guarantees that the global energy is a minimum, but does not guarantee the accuracy of the dislocation configurations at every instant. Thus, the deviation of an assumed spline shape form (i.e. kinematic constraint), may actually lead to an erroneous configuration if that configuration is close to a critical state (e.g. Orowan stress, flow stress for unlocking dislocations from cluster atmospheres, dipole and junction stability, etc). The basic question here is, therefore, how crude can one be in imposing the kinematic shape constraint for a specified level of temporal or spatial resolution? It is fairly obvious that the answer will depend on the mechanism at hand, and the level of detail for our description of such mechanism. To study the general accuracy and convergence of the PDD, we plan to present systematic studies of two broad categories of dislocation mechanisms: generation (including FR sources, and pileups), and hardening (including finite-size dipoles, junctions).

In section 2, we present a concise description of the PDD in a new dimensionless form. The temporal and spatial resolution of the PDD in a number of significant dislocation mechanisms will then be analysed in section 3, for both generation in section 3.1, and hardening in section 3.2. Finally, a discussion of these results and conclusions are given in section 4.

2. Dimensionless EOM for PDD

The method of PDD is described in sufficient detail in [29–33], and we will attempt here to give only a brief description for completeness. The first step is to calculate the stress field of curved parametric segments. Let the Cartesian orthonormal basis set be denoted by $\mathbf{1} \equiv \{\mathbf{1}_x, \mathbf{1}_y, \mathbf{1}_z\}$, $\boldsymbol{I} = \mathbf{1} \otimes \mathbf{1}$ as the second order unit tensor, and $\otimes$ denotes out tensor product. Now define the three vectors ($\boldsymbol{g}_1 = \boldsymbol{e}, \boldsymbol{g}_2 = \boldsymbol{t}, \boldsymbol{g}_3 = \boldsymbol{b}/|\boldsymbol{b}|$) as a covariant basis set for the curvilinear segment, and their contravariant reciprocals as [34]: $\boldsymbol{g}^i \cdot \boldsymbol{g}_j = \delta^i_j$, where δ^i_j is the mixed Kronecker delta and $V = (\boldsymbol{g}_1 \times \boldsymbol{g}_2) \cdot \boldsymbol{g}_3$ the volume spanned by the vector basis, as shown in figure 1. The parametric representation of a general curved dislocation line segment, shown in the figure, can be described by a parameter ω that varies from 0 to 1 at end nodes. The segment is fully determined as an affine mapping on the scalar interval $\{\omega \in [0, 1]\}$, if we introduce the tangent vector $\boldsymbol{T}$, the unit tangent vector $\boldsymbol{t}$, and the unit radius vector $\boldsymbol{e}$ as follows:

$$\boldsymbol{T} = \frac{\mathrm{d}\boldsymbol{l}}{\mathrm{d}\omega}, \qquad \boldsymbol{t} = \frac{\boldsymbol{T}}{|\boldsymbol{T}|}, \qquad \boldsymbol{e} = \frac{\boldsymbol{r}}{r}$$

Ghoniem *et al* [33] have shown that the elastic field of such a parametric segment can be obtained as an affine mapping transformation of the scalar parameter ω, and that the stress filed differential $\mathrm{d}\sigma$ introduced by a parametric differential $\mathrm{d}\omega$ are related as:

$$\frac{\mathrm{d}\boldsymbol{\sigma}}{\mathrm{d}\omega} = \frac{\mu V |\boldsymbol{T}|}{4\pi(1-\nu)R^2}\{(\boldsymbol{g}^1 \otimes \boldsymbol{g}_1 + \boldsymbol{g}_1 \otimes \boldsymbol{g}^1) + (1-\nu)(\boldsymbol{g}^2 \otimes \boldsymbol{g}_2 + \boldsymbol{g}_2 \otimes \boldsymbol{g}^2) - (3\boldsymbol{g}_1 \otimes \boldsymbol{g}_1 + \boldsymbol{I})\} \tag{1}$$

Once the parametric curve for the dislocation segment is mapped onto the scalar interval $\{\omega \in [0, 1]\}$, the stress field everywhere is obtained as a fast numerical quadrature sum from equation (1) [31].

To simplify the problem, let us define the following dimensionless parameters:

$$\boldsymbol{r}^* = \frac{\boldsymbol{r}}{a}, \qquad \boldsymbol{f}^* = \frac{\boldsymbol{F}}{\mu a}, \qquad t^* = \frac{\mu t}{B}$$

Here, a is lattice constant, $\boldsymbol{F}$ is resultant force which may consist of Peach–Koehler force [35] $\boldsymbol{F}_{\mathrm{PK}}$ (generated by the sum of the external and internal stress fields), the self-force $\boldsymbol{F}_s$ generated

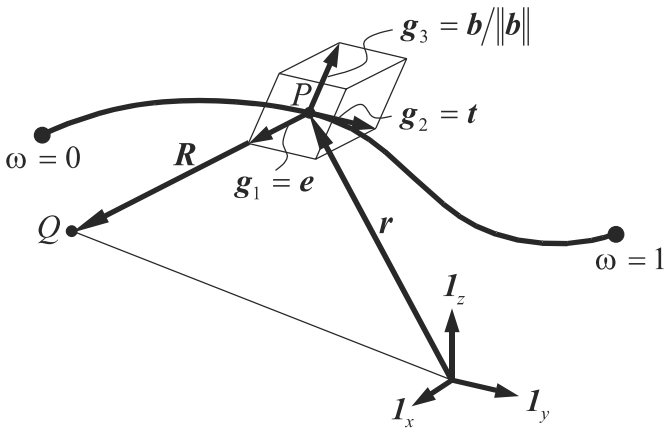

Figure 1. Parametric representation of a general curved dislocation segment, with relevant vectors defined (after [33]).

by local curvature at the point of interest. μ is shear modulus, and t is time. B is isotropic dislocation resistivity (inverse mobility). And following [32], a closed dislocation loop can be divided into N_s segments. In each segment j, we can choose a set of generalized coordinates q_m at the two ends, thus allowing parametrization of the form:

$$\boldsymbol{r}^* = \boldsymbol{C}\boldsymbol{Q} \tag{2}$$

Here,

$$\boldsymbol{C} = \begin{bmatrix} C_1(\omega) & 0 & C_2(\omega) & 0 & \cdots & C_m(\omega) & 0 \\ 0 & C_1(\omega) & 0 & C_2(\omega) & & 0 & C_m(\omega) \end{bmatrix},$$
$$C_i(\omega), \qquad (i = 1, 2, \ldots, m)$$

are shape functions dependent on the parameter ($0 \leqslant \omega \leqslant 1$), and $\boldsymbol{Q} = [q_1, q_2, \ldots, q_m]^\top$, q_i are a set of generalized coordinates. Substitute all these to the variational form of the governing EOM of a single dislocation loop [32], we obtain:

$$\sum_{j=1}^{N_s} \int_{\Gamma_j} \delta\boldsymbol{Q}^\top \left(\boldsymbol{C}^\top \boldsymbol{f}^* - \boldsymbol{C}^\top \boldsymbol{C} \frac{\mathrm{d}\boldsymbol{Q}}{\mathrm{d}t^*} \right) |\mathrm{d}\boldsymbol{s}| = 0 \tag{3}$$

Let,

$$\boldsymbol{f}_j = \int_{\Gamma_j} \boldsymbol{C}^\top \boldsymbol{f}^* |\mathrm{d}\boldsymbol{s}|, \qquad \boldsymbol{k}_j = \int_{\Gamma_j} \boldsymbol{C}^\top \boldsymbol{C} |\mathrm{d}s|$$

Following a similar procedure to the FEM, we assemble the EOM for all contiguous segments in global matrices and vectors, as:

$$\boldsymbol{F} = \sum_{j=1}^{N_s} \boldsymbol{f}_j, \qquad \boldsymbol{K} = \sum_{j=1}^{N_s} \boldsymbol{k}_j$$

then, from equation (3) we get,

$$\boldsymbol{K} \frac{\mathrm{d}\boldsymbol{Q}}{\mathrm{d}t^*} = \boldsymbol{F} \tag{4}$$

Equation (4) represents a set of ordinary differential equations, which describe the motion of an ensemble of dislocation loops as an evolutionary dynamical system. Generally, two numerical time integration methods are available for solving this set of equations: the implicit and the explicit classes of procedures. We will later discuss the accuracy and stability issues associated with each scheme.

In the applications presented here, we specifically use cubic splines as shape functions, and confine dislocation motion to be on its glide plane (i.e. the climb speed is negligible). Thus, we end up with only eight DOF for each segment with each node associated with four independent DOF. These cubic spline shape functions are given by

$$C_1 = 2\omega^3 - 3\omega^2 + 1$$
$$C_2 = \omega^3 - 2\omega^2 + \omega$$
$$C_3 = -2\omega^3 + 3\omega^2$$
$$C_4 = \omega^3 - \omega^2$$
$$\boldsymbol{Q} = [\boldsymbol{P}_1, \boldsymbol{T}_1, \boldsymbol{P}_2, \boldsymbol{T}_2]^\top$$

Here, $\boldsymbol{P}_i$ and $\boldsymbol{T}_i$ ($i = 1, 2$) correspond to the position and tangent vectors, respectively. In the following, we present results of studies for some of the main dislocation mechanisms to determine the effects of space and time discretization on the physical nature of the mechanism.

3. Spatial and temporal resolution of dislocation mechanisms

3.1. Dislocation generation

3.1.1. FR source. The FR mechanism of dislocation generation has been established as one of the primary processes which contribute to the increase in plastic strain upon application of a mechanical load. The main features of the mechanism have been documented in textbooks by hand sketches (e.g. [36–38]). More recently, details of its evolution have been utilized as implicit test beds to validate the numerical procedures of three-dimensional DD, outlined earlier in section 1 [17–23]. Because of the existence of these extensive studies, we will apply the PDD to analyse the evolution of FR sources, and show new aspects that are relevant to understanding the limitations of the PDD method in resolving spatial and temporal details. We examine in this section the following aspects of the FR source evolution: symmetry of stable and unstable sources, stable/unstable transition, shape accuracy as it depends on the number of segments (spatial resolution), solution stability (temporal resolution) and its dependence on time integration, adaptive nodal re-distribution techniques, and the accuracy of resolving dislocation annihilation and reconfiguration.

FR source symmetry and stability. The influence of the Burgers vector direction on the evolution of FR sources from an *initially straight* segment is determined in figure 2. A straight dislocation segment is pinned at two points ((−800, 0) and (800, 0)) in the local coordinate system of the (111) glide plane of an FCC metal, and is divided into 20 cubic spline segments. Although the results can all be given in dimensionless forms, it is instructive to use the properties of Cu for physical values. These are: $a = 0.36\,\text{nm}$, $B = 10^{-4}\,\text{Pa s}$, $\mu \approx 50\,\text{GPa}$, and $\nu = 0.31$. These values show that when the dimensionless time is 1000, the physical time is 2 ps. The segment is subjected to a sudden uniaxial stress σ_{11} (corresponding to a critical resolved shear stress (CRSS) τ/μ). σ_{11} is represented by a step function in time. In figure 2, $\boldsymbol{b} = \frac{1}{2}[\bar{1}10]$ is along the dislocation line sense vector, hence it represents a screw dislocation. For the sake of numerical studies, we select the vectors: $\boldsymbol{b} = (\sqrt{6}/3)[\bar{1}\bar{1}1]$ and $\boldsymbol{b} = \frac{1}{2}[\bar{1}01]$ to represent an edge and mixed dislocation, respectively, as shown in figure 2. The Burgers vectors are arbitrary in the latter two cases, but were introduced to ascertain the numerical aspects of FR symmetry during its expansion.

At the beginning, the curvature is almost zero everywhere and thus the effects of the self-forces are negligible. However, as the dislocation line bows out, the local curvature increases gradually, and then reaches its maximum value. In figure 2(*a*), the applied stress is relatively low ($\sigma_{11} = 80\,\text{MPa}$, or $\tau/\mu = 0.065\%$), thus the increase in the curvature everywhere eventually allows the self-force to balance the applied force and the FR source achieves an equilibrium shape. It is noted that the shape of the FR source is symmetric with respect to axis normal to its initial mid-point, for the initially pure screw and edge type of segments. The energy per unit length of a screw segment is lower than that for an edge segment. As a consequence, screw components tend to have higher self-forces (i.e. *stiffer*) than edge components. Figure 2 illustrates these features, where bowing out of initially screw dislocations is less pronounced than edge, both for the stable (figure 2(*a*)) and unstable (figure 2(*b*)) configurations. It is also noted that the FR source *stretches* along the Burgers vector direction for the mixed character case, as it tries to minimize its total elastic energy by increasing the length of its line along the screw (Burgers vector) direction.

Since the overall curvature of the FR source increases as it bows out, the applied stress must be increased to maintain successive equilibrium shapes. However, because the FR source is pinned at the two ends only, other configurations of lower curvature are possible, and can pass through the same two fixed points. As a consequence, the average curvature of the FR

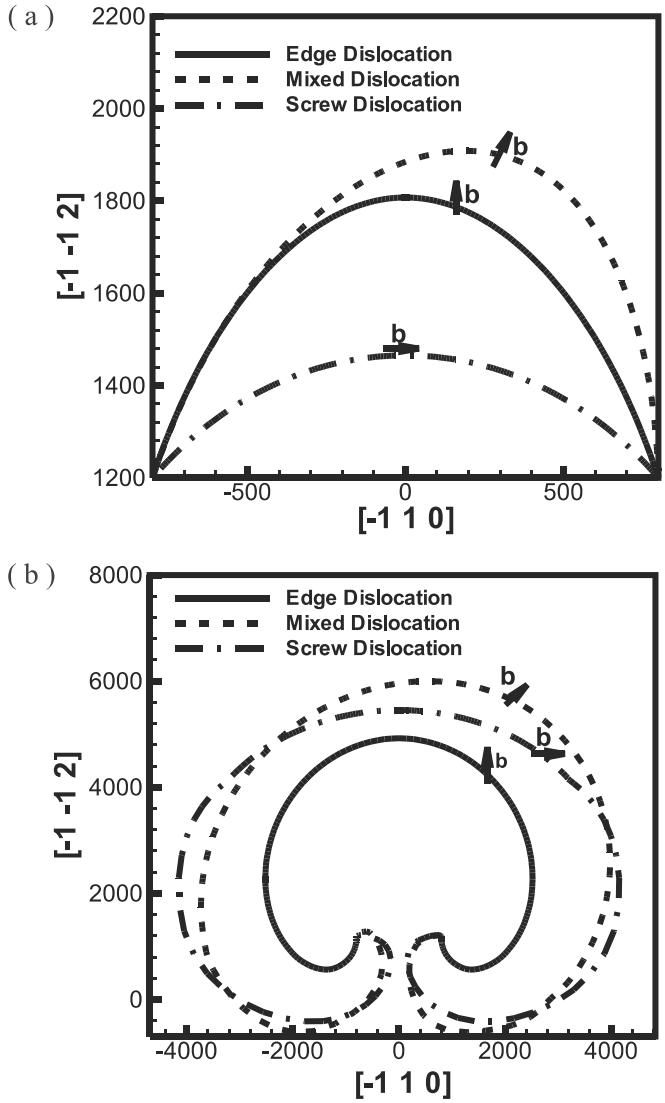

Figure 2. Effects of Burgers vector orientation on the evolution of an FR source in FCC crystals on the (111)-glide plane: (*a*) stable state ($\sigma_{11} = 80\,\text{MPa}$, $\tau/\mu = 0.065\%$); (*b*) unstable state ($\sigma_{11} = 200\,\text{MPa}$, $\tau/\mu = 0.16\%$). Burgers vectors are $(\sqrt{6}/3)[\bar{1}\bar{1}1]$(edge), $\frac{1}{2}[\bar{1}01]$(mixed), $\frac{1}{2}[\bar{1}10]$(screw), respectively at time $t^* = 4 \times 10^6$.

source reaches a maximum at a critical stress value (the Orowan stress), above which an unstable configuration of lower average curvature is reached. The transition from a stable FR configuration to an unstable one is illustrated in figure 2(*b*), where the applied stress is high ($\sigma_{11} = 200\,\text{MPa}$ ($\tau/\mu = 0.16\%$)), and the maximum self-force cannot balance the external driving force. Then dislocation will then continue expanding, which causes the curvature to decrease even further.

Resolution limits of the FR shape. For large-scale computer simulations, there is an obvious need to reduce the computational burden without sacrificing the quality of the physical results.

The smallest number of spline segments with the largest time step increment for integration of the EOM is a desirable goal. However, one must clearly identify the limits of this approach. We study here the influence of the nodal density on the dislocation line, and the time integration scheme on the ability to satisfactorily resolve the shape of a dynamic FR source. In order to estimate the error for different case, we define absolute error ϵ_a and relative error ϵ_r, respectively as follows:

$$\epsilon_a = \max \Delta r_i, \qquad i = 1, 2, \ldots, n$$
$$\epsilon_r = \left\{ \frac{1}{n} \sum_{i=1}^{n} \left(\frac{\Delta r_i}{r} \right)^2 \right\}^{1/2} \tag{5}$$

Here, $\Delta r_i = r_i - R$, which stands for ith sampling point of the position difference between current interpolation method and reference results. n is the total number of sampling points for calculating the error.

In figure 3, the dislocation line is divided into different number of segments, and the FR source is evolved by numerical integration. Different applied external stress is applied to the dislocation. Figure 3(a) is correspond to low applied stress $\sigma_{11} = 80\,\text{MPa}$ ($\tau/\mu = 0.065\%$) with final stable configurations. It is shown that one can achieve very high precision in describing the stable FR shape with very small number of segments. The corresponding error is shown in table 1. The reference configuration is chosen as that with 30 segments (thus the relative and absolute error is set to zero). It is found that with the number of segments increased, both the relative and absolute error decreased sharply, while the running time increased significantly. It is interesting to note here that with only two segments, one can achieve almost the same resolution as that of 30 segments, the relative error is less than 0.2%, while the running time is trivial compared with that with 30 segments, only 2%. However, when the FR source becomes unstable, the variation of curvature is considerable between its middle section and the sections close to the pinning points. Figure 3(b) and table 2 show the configuration and corresponding absolute, relative error and running time respectively at higher applied stress $\sigma_{11} = 200\,\text{MPa}$ ($\tau/\mu = 0.16\%$). The error estimation is shown in table 2 (in this particular case the reference configuration is chosen as that with 40 segments). It is found that with only two segments the method is unable to achieve high accuracy, although it still converges. The unstable configuration is more complicated, since the curvature is much higher at the zone near fixed points. Hence, two segments are not sufficient to to capture such curvature variation within the cubic spline shape function framework. It is shown in table 2 that with increasing the number of segments, the accuracy increases significantly, albeit at the expense of an increase in computing time.

The influence of the time integration method on the shape convergence of the FR source is studied in figure 4, and its corresponding error estimation is shown in table 3. The same conditions as in figure 3 are chosen, except that the applied uniaxial stress $\sigma_{11} = 70\,\text{MPa}$ ($\tau/\mu = 0.056\%$). The results of shape evolution for the explicit integration with different time steps are compared to those obtained with an implicit scheme. One-step Euler forward integration explicit scheme is utilized. In the explicit scheme, it is noted that when the time step is larger than $\approx$3000, a numerical shape instability sets in. For the parameters chosen here, this corresponds to a physical time step of $\approx$6 ps. The shape tends to diverge more along screw segments of the FR source. For a time step on the order of 1000 (i.e. $\Delta t \approx 2\,\text{ps}$), the FR shape is numerically stable, but not accurate. Finally, the FR source shape converges (i.e. accurate and stable), when the explicit time step is less than 500 (i.e. $\Delta t \approx 1\,\text{ps}$). Such small limit on the time step for high mobility crystals (e.g. FCC metals) can result in severe restrictions on the ability of current day computers to simulate plastic deformation of large

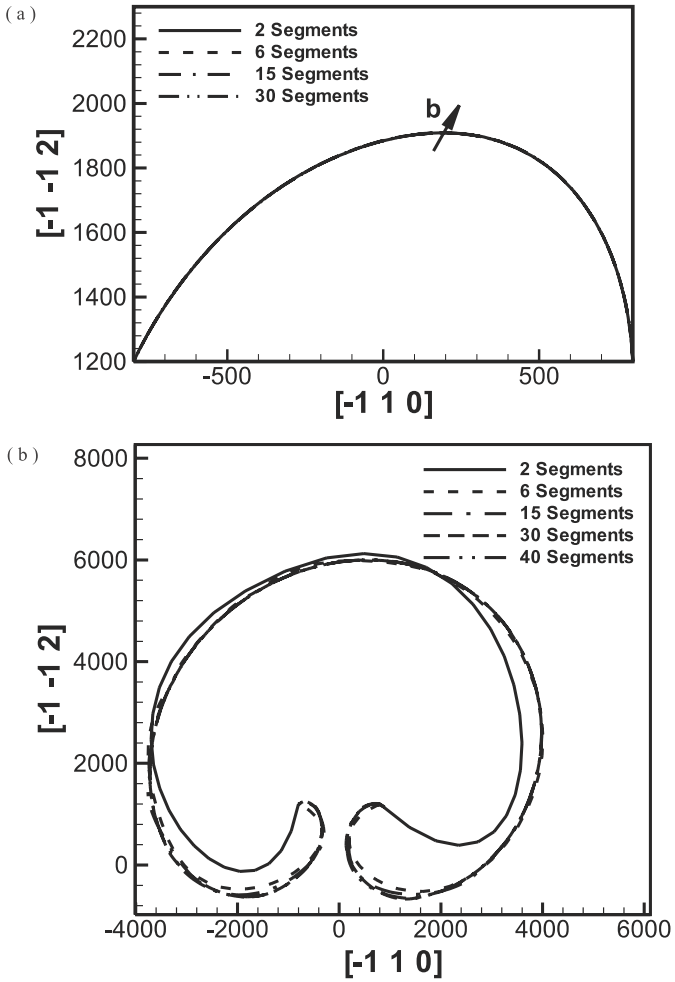

Figure 3. The influence of number of segments on the shape convergence of an FR source with Burgers vector $\frac{1}{2}[\bar{1}01]$ at different stress levels: (*a*) stable state ($\sigma_{11} = 80$ MPa, $\tau/\mu = 0.064\%$), (*b*) unstable state—same time: ($\sigma_{11} = 200$ MPa, $\tau/\mu = 0.16\%$).

Table 1. Error estimation for stable state FR source.

No. of segments	Absolute error ϵ_a	Relative error ϵ_r (%)	Runtime (s)
2	6.06	0.17	0.12
6	6.01	0.15	0.42
15	1.32	0.018	1.53
30	0	0	5.77

volumes to realistic experimental time. An implicit integration method developed by Gear [40] is also used to test the same problem. The method is designed for the numerical integration of stiff, ordinary differential equations, with a variable time step that is automatically determined on the basis of the fastest variation of any of the DOF. A level of relative accuracy of 10^{-6} is selected as a convergence constraint. Since the time step is automatically adjusted to capture the specified level of accuracy, the overall scheme is stable and convergent. From table 3, it is

Table 2. Error estimation for unstable FR source at $t^* = 5 \times 10^6$.

No. of segments	Absolute error ϵ_a	Relative error ϵ_r (%)	Runtime (s)
2	1408.8	20.15	0.02
6	191.1	5.04	0.20
15	133.8	3.24	2.53
30	142.0	2.93	24.14
40	0	0	27.57

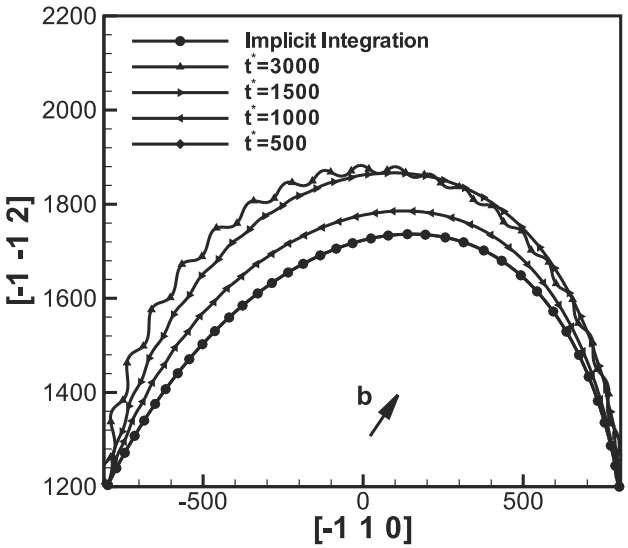

Figure 4. The influence of the time integration scheme on the shape convergence of an FR source. The calculation condition is chosen the same as that in figure 3, except the applied stress $\sigma_{11} = 70\,\text{MPa}$, $\tau/\mu = 0.056\%$.

Table 3. Error estimation for different integration schemes. The implicit scheme is chosen as the reference configuration for error estimation.

Integration scheme	Absolute error ϵ_a	Relative error ϵ_r (%)	Runtime (s)
Explicit int. ($\Delta t^* = 3000$)	168.4	6.11	0.92
Explicit int. ($\Delta t^* = 1500$)	141.5	5.40	1.82
Explicit int. ($\Delta t^* = 1000$)	56.90	2.34	2.76
Explicit int. ($\Delta t^* = 500$)	0.06	0.003	5.68
Implicit integration	0	0	1.52

noted that the overall computational time in implicit integration is much less than that in the explicit integration scheme of comparable accuracy and stability. This is due to the ability to adjust the time step during implicit integration in accordance with the stiffness of the equations, while the stability demands of the explicit Euler method require very small time steps.

Adaptive node re-distribution. To capture details of small-scale processes, such as the interaction between a dislocation and an atomic size defect cluster, or during the annihilation reaction between two dislocation segments of the same Burgers vector and of opposite tangent

vectors, large variations of the local dislocation line curvature would be expected. To effectively resolve these or similar mechanisms, we develop here a protocol for adaptively re-distributing the nodal density on the dislocation line according to the variation in the local curvature. To show the level of resolution gained by this protocol, we study here the mechanism of dislocation segment annihilation in an expanding FR source, and the subsequent generation of a fresh and closed dislocation loop. Figure 5 shows the details of this of segment annihilation and the ensuing recovery process of a fresh closed loop, generated from an asymmetric FR source. The simulation conditions are the same as in figure 3, except that with different applied uniaxial stress $\sigma_{22} = 140\,\text{MPa}$ ($\tau/\mu = 0.112\%$), and the Burgers vector of the loop is $\boldsymbol{b} = \frac{1}{2}[0\bar{1}1]$.

In order that one can resolve the annihilation event, the distance between any two nodes is tracked, and when the minimum distance between two segments of opposite tangent vectors is below a prescribed limit (e.g. 100), the time step is reduced and the integration proceeds further till the two segments are a distance of 1–2 apart. The nodes are then re-distributed in the immediate region, resulting in two separate loops, as can be seen in figure 5. After the annihilation event takes place, both new loops generate cusp regions, where the curvature is extremely high. It is highly desirable to develop an adaptive method, which can resolve such essential physical phenomena to sufficient accuracy without excessive computations.

In present algorithm, nodal re-distribution is invoked at prescribed time intervals, not necessarily related to the integration time step, as follows. Each cubic spline segment is divided into several sub-segments with equal arc length, and new ghost nodes are assigned. Thus, the entire loop is now filled with ghost nodes of equal nodal density per unit line length. Note that the total number of DOF for the loop is not changed up till this point. Also, the average loop curvature κ_{avg} is determined simply as the mean value of the maximum $\kappa_{\max}$, and minimum $\kappa_{\min}$ curvatures of all ghost nodes. Now, in order to increase the nodal density per unit arc length for high curvature regions, we start from one end of the loop that has a current

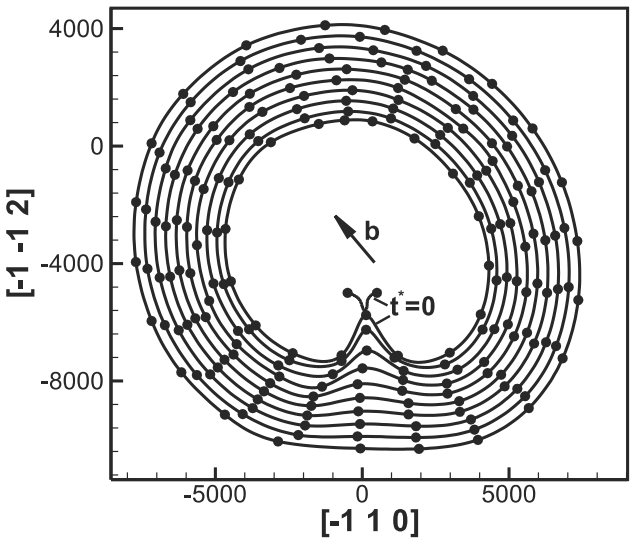

Figure 5. Expansion of an initially mixed dislocation segment in an FR source under the step function stress of $\sigma_{22} = 140\,\text{MPa}$ ($\tau/\mu = 0.112\%$). The FR source is on the (111)-plane of a Cu crystal with Burgers vector $\boldsymbol{b} = \frac{1}{2}[0\bar{1}1]$. The time interval between different contours is $\Delta t^* = 5 \times 10^5$.

curvature κ, and skip a number of ghost nodes N_{skip} determined by the relation:

$$N_{\text{skip}} = C\left(\frac{\kappa_{\text{avg}}}{\kappa}\right) \tag{6}$$

C is an adjustable constant that determines the relationship between the line nodal density and the local curvature. Thus, in this protocol, more nodes are added to the zone with high curvature while in the low curvature zone, less nodes are added. In figure 5, node re-distribution is shown in each closed loop. The total number of nodes in each loop at a given time is generally kept under 25.

3.1.2. Dislocation pileups. Dislocation generation by the FR mechanism leads to an increase in the dislocation density, and hence the total strain. This does not go on perpetually, because generated dislocation loops interact with various obstacles, and can be totally immobilized. Grain boundaries represent such strong obstacles to dislocation motion, and have a strong effect on the subsequent dynamics of dislocation loops emitted from FR sources. Strong grain boundaries can confine dislocations within its grain. If the FR source continues to emit dislocations, new loops will interact with the immobilized leading dislocation, and as a result will form a *dislocation pileup*. The single crystal is represented by a cube, 30 000 (or 10 μm) in length. One FR source of an initially mixed dislocation character, with Burger's vector $\frac{1}{2}[0\bar{1}1]$, under an applied uniaxial stress $\sigma_{22} = 140$ MPa ($\tau/\mu = 0.112\%$), will emit closed dislocation loops continuously. Since the grain boundary is assumed to be rigid, once the first closed loop reaches the grain boundary, the position of the node will be confined inside the boundary due to the strong obstructive force. The position vector of node in closed dislocation loop will be fixed. The subsequent loop will be confined to the previous loop due to its repulsive force. Figure 6 shows the formation of a three-loop pileup from the same FR source. The same nodal re-distribution strategy is used for each closed loop in order to get higher accuracy.

3.2. Hardening mechanisms

3.2.1. Dipole formation. In all previous applications of the PDD, strong interactions between different loops is not a major factor that determines the final outcome of each mechanism, although in the case of a dislocation pileup, moderate loop reconfiguration takes place as a result of loop–loop interaction. For large-scale computer simulations of dislocation ensembles [33], loop–loop and loop-obstacle interactions determine the rate of strain hardening

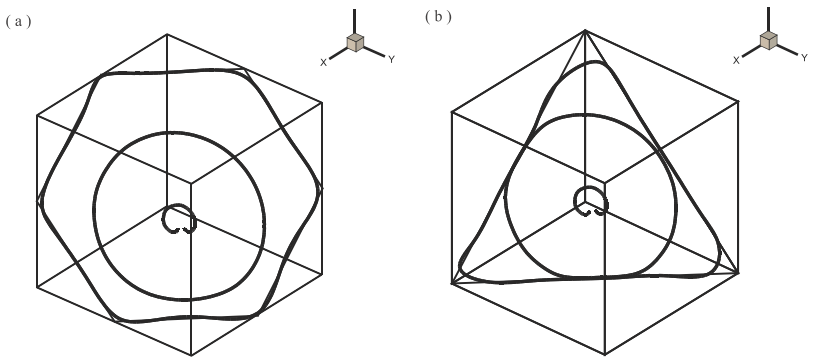

Figure 6. The effects of a rigid grain boundary of triangular cross-section in Cu on the evolution of a closed dislocation loop emanating from an FR source. The external uniaxial stress $\sigma_{11} = 120$ MPa ($\tau/\mu = 0.096\%$). The glide plane in s (111), and the Burgers vector is $\boldsymbol{b} = \frac{1}{2}[0\bar{1}1]$.

or softening [32]. We consider here several interaction mechanisms that are dominant in various stages of strain hardening. These are dipole formation and breakup, and the formation and destruction of dislocation junctions.

Finite-size dipole formation and destruction. It has been pointed out [5] that the destruction of dislocation dipoles plays a significant role in the evolution of persistent slip bands (PSB) under fatigue loading conditions. Dislocation dipoles play significant roles in a host of hardening mechanisms, and thus conditions for their formation and destruction must be worked out. The stability of very long dipoles has been determined from static equilibrium considerations, and the shear stress necessary to destabilize a dipole of a given width, h, is given in [41].

The more general dynamic stability conditions of infinite length dipoles have been determined by Huang *et al* [42]. Here, we focus on the accuracy of the dynamics of formation and breakup of finite-size dipoles in FCC metals. Figure 7 shows a two-dimensional projection on the (111)-plane of the dynamic process finite-size dipole formation. Two initially straight dislocation segments with the same Burgers vector $\frac{1}{2}[\bar{1}01]$, but of opposite line directions are allowed to glide on nearby parallel $\{111\}$-planes without the application of an external stress. The two lines attract one another, thus causing the two loop segments to move and finally reach an equilibrium state of a finite-size dipole. The two parallel dislocations are pined at both ends, the upper loop glides on the 'top' plane, while the lower one glides on the 'bottom' plane, as shown in figure 7. The mutual attraction between the two dislocations becomes significant enough to simultaneously reconfigure both of them only during the latter stages of the process. Because the two dislocations start with a mixed character, a straight and tilted middle section of the dipole forms. The length of this middle section, which we may simply ascribe as the dipole length, is only determined by the balance between the attractive forces on the middle straight section, and the self-forces on the two end sections close to the pinning points. The separation of the two planes is $25\sqrt{3}$, which is approximately 60 $|\boldsymbol{b}|$.

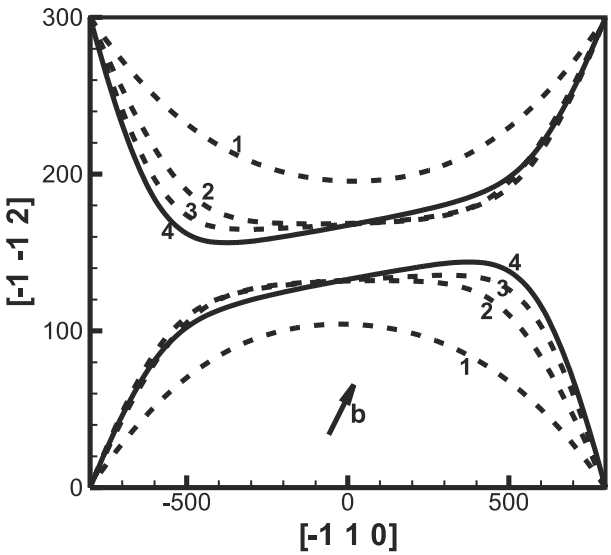

Figure 7. Two FR source dislocations with the same Burgers vector ($\boldsymbol{b} = \frac{1}{2}[\bar{1}01]$) but opposite tangent vectors gliding on two parallel (111)-planes (distance $h = 25\sqrt{3}a$ apart) form a short dipole in an unstressed state. The view is projected on the (111)-plane. Time intervals are: (1) 2.5×10^5; (2) 4.75×10^5; (3) 5×10^5; (4) equilibrium state.

The error estimation of different nodal distribution of the dipole is shown in table 4. It is shown that with only two segments each dislocation, we can get as high accuracy as with 20 segments, the relative error is less than 5%.

Finite-size dipoles will be stable on their own, so long as perturbing external or internal stress fields are not present. It is immediately obvious from figure 7 that the dipole configuration is *symmetric* with respect to the direction of an applied shear stress parallel to the two glide planes. Calculations of dipole dynamics under the influence of an externally applied stress show that it is much easier to *unzip* the dipole in the reverse direction than to destroy it in the forward direction. Figure 8 summarizes the relationship between the unzipping stress and the inverse of the inter-planar distance $1/h^*$. A comparison is also made in the same figure with stress values needed to destabilize an infinite dipole calculated by [41], and the values needed to destroy it in the forward direction.

As a result of the self-forces generated by the curvature of the two end sections of the dipole, the unzipping strength is a factor of two smaller than the strength of an infinite dipole. In the forward destruction case, however, the self-forces tend to hold both dislocations back, thus a higher external stress is needed to break up the dipole. The present results are calculated for an initial horizontal separation of 350 for the two straight segments before the dipole forms.

Table 4. Error estimation for different nodal distributions for dipole formation. The configuration with 20 segments on each dislocation is chosen as the reference configuration.

No. of segments	Absolute error ϵ_a	Relative error ϵ_r (%)	Runtime (s)
2	26.5	3.16	12.7
4	18.6	2.37	43.3
5	7.8	1.13	84.9
10	3.6	0.36	438.2
20	0	0	1503.1

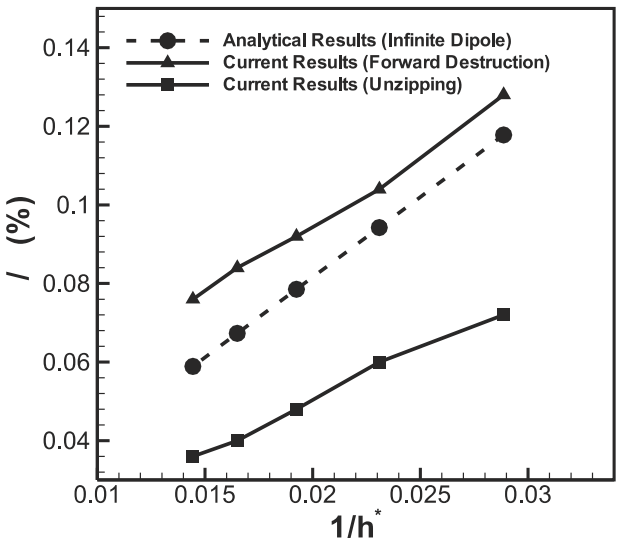

Figure 8. The relative shear stress (τ/μ) to break up a finite-size dipole as a function of the relative inverse separation $1/h^*$, $h^* = h/a$. h is the distance between the two parallel planes. The distance between the pinning points of the two FR sources $L = 1600a$, and they are originally separated by $350a$ horizontally.

Increasing this distance results in smaller effects of the curved sections of the dipole, and hence both unzipping and forward destruction stresses approach the infinite dipole values. It is to be noted here that all these results are for static dipoles, or for initial dislocation velocities smaller than $\frac{1}{2}$ the transverse sound speed. The stability of the dynamic infinite dipole is treated in [42].

3.2.2. Dislocation junctions. Dislocation–dislocation interaction can result in either their attraction towards each other, or their repulsion from one another. The interaction of dislocations at close separation has been found to be associated with significant reconfiguration of their shapes [25–27]. If dislocation interaction is attractive, the two closest segments are simultaneously pulled towards each other till a stable common part (junction) of the two dislocations is formed. However, when the segments repel one another, a stable crossed state can also form [44]. The dynamics of dislocation junction formation and breakup have attracted recent attention (e.g. [26,45]), because of the importance of this mechanism in strain hardening and pattern formation [5]. Especially in FCC metals of low stacking fault energy, dislocation junction structures are usually complex, since dislocation cores are dissociated into partials separated by stacking faults [38]. Under these conditions, sessile Lomer–Cottrell junctions are generated. They significantly impede further dislocation motion resulting in strain hardening. Also, undissociated locks (Lomer dislocations) can significantly impede dislocation motion. Because of their stability, sessile junctions can also act as nucleation sites for dislocation cell walls [5]. In the present PDD method, we introduce a critical length scale $r_c \approx |\boldsymbol{b}|$, where the two dislocation cores are not permitted to interpenetrate if they approach one another at smaller distances. In this simple fashion, complex atomic level simulation of the core structure is obviated [45], and no specific rules are further introduced.

First, we show in figure 9 the dynamics of attractive junction formation without any externally applied stress. Two initially straight dislocations of Burgers vectors and slip planes given by: $\boldsymbol{b}_1\boldsymbol{n}_1 = \frac{1}{2}[01\bar{1}](111)$ and $\boldsymbol{b}_2\boldsymbol{n}_2 = \frac{1}{2}[101](11\bar{1})$ are pinned at their ends, and allowed to move approaching each other until they are locked at equilibrium. Their locked equilibrium state can be understood to result from the balance between their mutual interaction at the close separation of r_c, and the respective self-forces of their curved arms that form close to the pinned ends. The length of the straight section (junction) that forms at the intersection of the two glide planes is approximately 200. Figure 9(*a*) shows a two-dimensional projection view of the successive motion of $\frac{1}{2}[01\bar{1}](111)$, while the three-dimensional view of the junction structure is shown in figure 9(*b*). In order to calculate the error generated by different nodal distribution, the configuration with 12 nodes each dislocation is set as the reference one. The error estimation is shown in table 5. It is shown that with less than eight segments, one can get good shape junction.

The intrinsic strength of junctions is the key factor in understanding strain hardening in crystals [36], thus it is important to study the process of junction destruction under an externally applied stress. Once an unstressed junction is formed, as shown earlier here, the binding forces on its middle straight section will be balanced by the self-forces on the four curved arms. However, if an applied stress is also introduced, the balance of forces is very delicate, because the dislocation curvature at both ends of the straight junction section changes considerably. The two ends of the junction act as pseudo-pinning points, and the four arms start to behave like the normal FR sources at their earlier stages (i.e. bowing out considerably as the applied stress is gradually increased). The difference is that these two points are not really fixed as in common FR sources. Self-forces caused by dislocation curvature generate a shear force on the two pseudo points forcing them to move inward. The destruction process can be viewed as the competition between dislocation core forces, which stabilize the junction and counter shear

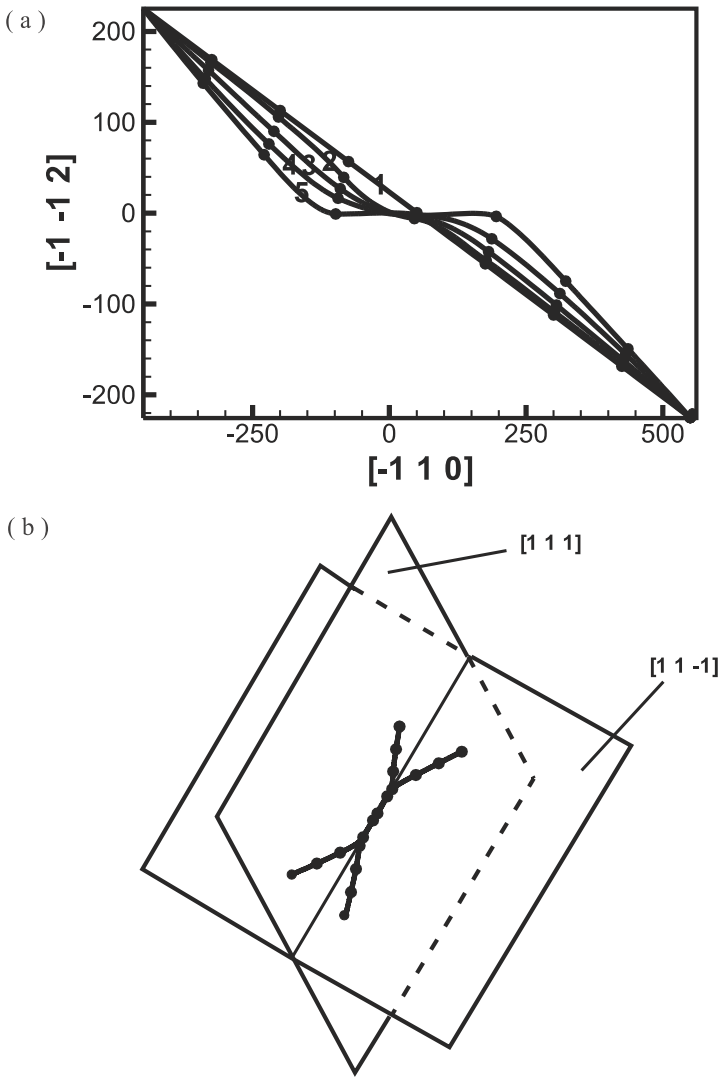

Figure 9. Dynamics of 2 unstressed FR sources ($\frac{1}{2}[01\bar{1}](111)$ and $\frac{1}{2}[101](11\bar{1})$) forming a three-dimensional junction along $(\bar{1}10)$, $\boldsymbol{b} = \frac{1}{2}[110]$. (*a*) Two-dimensional view for the motion of the FR source ($\frac{1}{2}[01\bar{1}](111)\frac{1}{2}[\bar{1}01](1\bar{1}1)$) on its glide plane (111). Time intervals are: (1) initial configuration; (2) 1.5×10^4; (3) 5.0×10^4; (4) 1.3×10^5; (5) final configuration. (*b*) Three-dimensional view of the junction.

forces on the two pseudo-pining points. Figure 10 shows the detailed dynamics of junction unzipping under an increasing applied stress σ_{11}/μ. It is interesting to point out that, when the applied stress is gradually increased, with the bowing out of the four arms, the curvature near pseudo-pinning points becomes high, resulting in a reduction of the junction length by the inward motion of the end points of the junction. As a consequence, the entire junction becomes unstable. At lower applied stress $\sigma_{11}/\mu = 0.2\%$, the shear force on the two end points of the junction can be balanced by the high junction binding forces. A final equilibrium state is generated, but with a shorter junction length, as shown in figure 10(*a*). When σ_{11}/μ

Table 5. Error estimation for different nodal distributions for junction formation. The configuration with 12 segments on each dislocation is chosen as the reference configuration.

No. of segments	Absolute error ϵ_a	Relative error ϵ_r (%)	Runtime (s)
3	27.8	20.05	406.2
4	19.7	14.25	841.1
6	16.0	8.75	2932.6
8	4.97	1.00	4902.4
12	0	0	8320.2

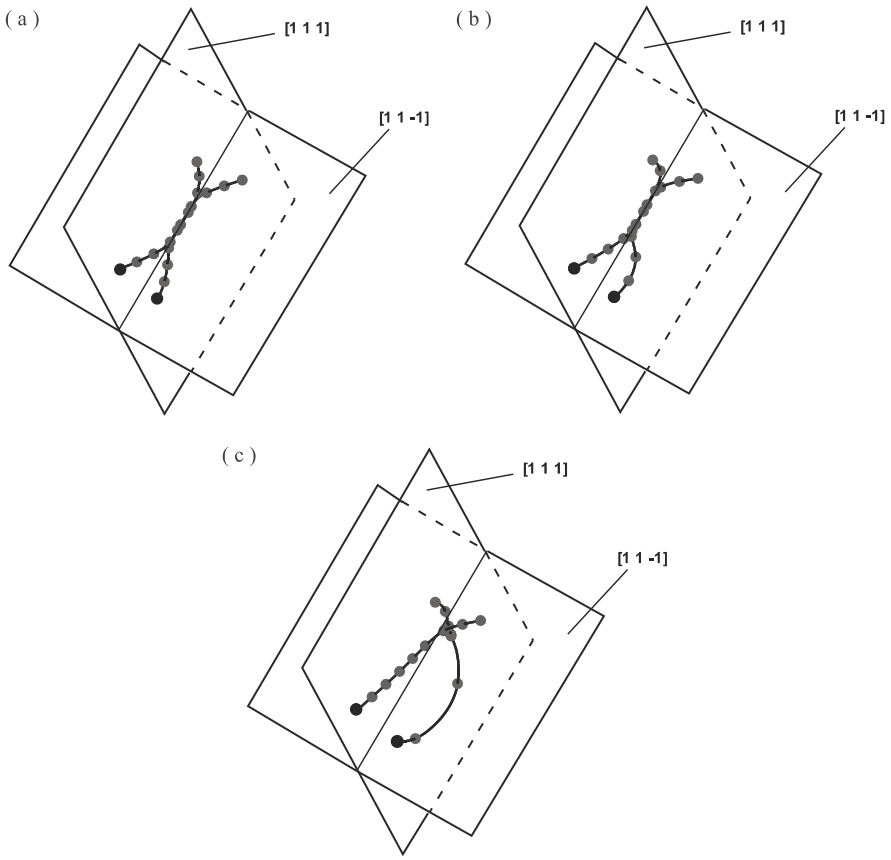

Figure 10. Dynamics of a *stressed* junction showing configurations at various stress levels: (*a*) equilibrium, $\sigma_{11} = 100$ MPa ($\sigma_{11}/\mu = 0.2\%$). (*b*) Equilibrium, $\sigma_{11} = 250$ MPa ($\sigma_{11}/\mu = 0.5\%$). (*c*) Unstable, $\sigma_{11} = 300$ MPa ($\sigma_{11}/\mu = 0.6\%$).

is increased to 0.6%, the shear force reaches a critical value, which can no longer be balanced by binding forces, and a dynamically unstable *unzipping* process ensues at both ends of the junction till it totally breaks up, and the two dislocations are freed from one another. The high spatial and temporal fidelity of the PDD is clear in this example, since only 5–9 segments are used throughout the entire simulation. The simulation encompasses balance between binding forces as a result of interaction between straight segments within the junction separated by only one atomic distance, and forces on the arms of the curved segments at much larger length scales with only a few segments. The results obtained here with a few DOF for the dynamics

of junction formation and destruction are in general agreement with the atomistic simulation of Rodney and Philips [45].

4. Conclusions and discussion

The three-dimensional nature of dislocation processes in deforming metals is quite complex. Because of the enormous range of applications possible with three-dimensional DD, the field has progressed very rapidly in recent years. Before integration of many of the dislocation mechanisms in large-scale computer simulations, it is quite relevant to investigate the numerical issues of accuracy, convergence and stability, so that large-scale computer simulations can be reliably utilized in studies of micro- and meso-scale plasticity. This work attempts to present a comprehensive investigation of some of the fundamental mechanisms involved in the dynamics of three-dimensionally interacting dislocations. The aim is two fold: (1) to focus on the specific method of PDD and explore how far it can be used to resolve spatial and temporal events during the course of dislocation interactions; (2) to unravel physical phenomena that determine the outcome of salient dislocation mechanisms.

Numerical studies of dislocation generation by the FR mechanism revealed a number of significant features. The shape accuracy (defined as relative deviation from a convergent shape) of an equilibrium FR source has been shown to be excellent with only a few parametric segments. With only two segments, a maximum relative accuracy of 10^{-3} can be achieved. The shape accuracy of an unstable FR source requires a larger number of segments, and six segments produce similar accuracy. The shapes of both equilibrium and unstable FR sources were shown to absolutely converge as the number of segments is increased. However, resolution of the annihilation event and subsequent loop reconfiguration requires adaptive node re-distribution and a higher nodal density on the dislocation line at regions of high curvature. It is also shown that while implicit integration of the EOM produces stable solutions, the explicit integration scheme requires more care. As the time step in the explicit method is increased, numerical instabilities set in. For a numerically stable solution, the time step has to be reduced to less than 500 dimensionless units (on the order of 1 ps for a mobility of $10^4\,\mathrm{Pa}^{-1}\,\mathrm{s}^{-1}$). For such a small time step and a relative accuracy of 10^{-6}, implicit integration of the EOM is found to be generally faster by up to 1 orders of magnitude. For isotropic mobility on the glide plane, it is shown that when the Burgers vector is inclined with respect to the initial tangent vector, the FR source shape is elongated in the Burgers vector direction so as to minimize the elastic energy of the loop, even in highly dynamic conditions. When dislocations are generated inside grains with rigid boundaries, it is shown that the dislocation shape adjusts to the shape of the grain boundary. The radius of curvature of these dislocation sections is inversely proportional to the CRSS on the slip plane. The leading dislocation emitted by an FR source expands first to the closest boundary, and then gradually fills in the outline of the grain boundary. Subsequent emitted loops are found to be more curved and less conforming to the boundary shape,and they form a well defined dislocation pileup.

For the hardening mechanisms investigated: dipoles and junction formation, a number of significant features have been found. In the case of a finite-size dipole, with only 2 segments on each dislocation, the formation and destruction dynamics are resolved with a relative accuracy of less than 10^{-2}. The formation dynamics reveal that the two interacting dislocations do not feel one another till their closest segments are within $\approx$100. The finite dipole shape then changes very rapidly achieving equilibrium conditions from that point in less than 10^5 dimensionless time units ($\approx$200 ps). Fairly long straight sections are formed on the FR source with screw orientations, perhaps promoting cross-slip communication between the two FR sources, and possibly forming a dipolar loop. This possibility needs further investigation as a

cause of dipolar loop formation. It is found that the stress to *unzip* the dipole is smaller than the breakup stress of infinite size dipoles, nearly by a factor of 2. On the other hand, to break up the dipole by pushing the two dislocations past one another (forward destruction) requires a stress that is nearly 30% higher than the infinite dipole.

Studies of the process of unstressed sessile junction formation with PDD, and its destruction by an externally applied stress has been consistent with similar recent studies with other methods. However, the number of required segments for spatial resolution of less than 10^{-3}, and for temporal resolution of 10^{-6} requires only eight segments per interacting dislocation. When an external stress is applied to a stable junction, the two ends of the junction behave as anchor points for four *pseudo* FR-sources. The stress causes the FR sources to bow out thus increasing the reverse force at the anchors and simultaneously moving them inwardly to shorten the length of the junction. When the stress reaches a critical value, the speed of motion of the two anchors towards one another increases and the whole junction collapses. Each two of the *pseudo* FR-sources join together forming only two freed FR sources that expand by the usual mechanism.

Acknowledgments

Research is supported by the US Department of Energy, Office of Fusion Energy, through Grants DE-FG03-98ER54500 and DOE Grant DE-FG03-00ER54594 with UCLA.

References

[1] Lepinoux J and Kubin L P 1987 *Scr. Mater.* **21** 833
[2] Ghoniem N M and Amodeo R 1988 *Solid State Phenomena* **3&4** 377
[3] Guluoglu A N, Srolovitz D J, LeSar R and Lomdahl R S 1989 *Scr. Mater.* **23** 1347
[4] Amodeo R J and Ghoniem N M 1990 *Phys. Rev.* B **41** 6958
[5] Amodeo R J and Ghoniem N M 1990 *Phys. Rev.* B **41** 6968
[6] Amodeo R J and Ghoniem N M 1991 Rapid algorithms for dislocation of dynamics in micromechanical calculations *Modeling of Deformation of Crystalline Solids* ed T Lowe, T Rollett, P Follansbee and G Daehn (TMS Press) p 125
[7] Groma I and Pawley G S 1993 *Phil. Mag.* A **67** 1459
[8] Lubarda V A, Blume I A and Needleman A 1993 *Acta Metall. Mater.* **41** 625
[9] Wang H Y and Lesar R 1995 *Phil. Mag.* A **71** 149
[10] Barts D B and Carlsson A E 1995 *Phys. Rev.* E **52** 3195
[11] Raabe D 1998 *Phil. Mag.* A **77** 751
[12] Kubin L P, Canova G, Condat M, Devincre B, Pontikis V and Brechet Y 1992 *Solid State Phenomena* **23/24** 445
[13] Kubin L P and Canova G 1992 *Scr. Metall.* **27** 957
[14] Devincre B and Condat M 1992 *Acta Metall. Mater.* **40** 2629
[15] Canova G, Brechet Y and Kubin L P 1992 *Modeling of Plastic Deformation and its Engineering Applications* ed S I Anderson *et al* (Roskilde, Denmark: RISØ National Laboratory)
[16] Kubin L P 1993 *Phys. Status Solidi* a **135** 433
[17] Canova G, Brechet Y, Kubin L P, Devincre B, Pontikis V and Condat M 1993 *Microstructures and Physical Properties* ed J Rabiet, CH-Transtech
[18] Devincre B and Kubin L P 1994 *Model. Simul. Mater. Sci. Eng.* **2** 559
[19] Devincre B 1996 Meso-scale simulation of the dislocation dynamics *Computer Simulation in Materials Science* ed H O Krichner *et al* (Dordrecht: Kluwer) p 309
[20] Devincre B and Kubin L 1997 *Philosophical Transactions of the Royal Society London, Series A* vol 355 (UK: Mathematical, Physical and Engineering Sciences) p 2003
[21] Moulin A M, Condat P and Kubin L 1997 *Acta Mater.* **45** 2339
[22] Hirth J P, Rhee M and Zbib H 1996 *J. Computer-Aided Mater. Design* **3** 164
[23] Zbib H M, Rhee M and Hirth J P 1998 *Int. J. Mech. Sci.* **40** 113
[24] Yoffe E H 1960 *Phil. Mag.* **5** 161
[25] Schwarz K W and Tersoff J 1996 *Appl. Phys. Lett.* **69** 1220

[26] Schwarz K W 1997 *Phys. Rev. Lett.* **78** 4785
[27] Schwarz K W and LeGoues 1997 *Phys. Rev. Lett.* **79** 1877
[28] Brown L M 1967 *Phil. Mag.* **15** 363
[29] Ghoniem N M 1999 *J. Eng. Mat. Tech.* **121** 136
[30] Kukta R V and Freund L B 1998 Multiscale modelling of material *MRS Proc.* ed V V Bulatov, Tomas Diaz de la Rubia, R Phillips, E Kaxiras and N Ghoniem (Massachusetts, USA: Boston)
[31] Ghoniem N M and Sun L Z 1999 *Phys. Rev.* B **60** 1
[32] Ghoniem N M, Tong S-H and Sun L Z 2000 *Phys. Rev.* B **61** 913
[33] Ghoniem N M, Huang J and Wang Z 2002 Affine covariant-contravariant vector forms for the elastic field of parametric dislocations in isotropic crystals *Phil. Mag. Lett.* **82** 55–63
[34] Holzapfel G 2000 *Nonlinear Solid Mechanics* (West Sussex, England: Wiley) p 36
[35] Peach M O and Koehler J S 1950 *Phys. Rev.* **80** 436
[36] Friedel J 1964 Dislocations (Oxford: Pergamon)
[37] Hirth J P and Lothe J 1982 *Theory of Dislocations* 2nd edn (New York: McGraw-Hill)
[38] Hull D and Bacon D J 1977 *Introduction to Dislocations* 3rd edn (Linacre House, Jordan Hill, Oxford: Butterworth-Heinemann)
[39] Amodeo R J and Ghoniem N M 1998 *Int. J. Eng. Sci.* **26** 653
[40] Gear C W 1971 *Numerical Initial Value Problems in Ordinary Differential Equations* (Englewood Cliffs, NJ: Prentice-Hall)
[41] Zbib H M, Diaz de la Rubia T, Rhee M and Hirth J P 2000 *J. Nucl. Mater.* **276** 154
[42] Huang H, Ghoniem N M, Diaz de la Rubia T, Rhee M, Zbib H and Hirth J 1999 *J. Eng. Mater. Technol.* **121** 143
[43] Kubin L P and Kratochvil J 2000 *Phil. Mag.* A **80** 201
[44] Schwarz K W 2001 *J. Mat. Sci. Eng.* A **309** A310
[45] Rodney D and Phillips R 1999 *Phys. Rev. Lett.* **82** 1704

Summary of Comments on msm155385

Page: 18

Sequence number: 1
Author:
Date: 11/14/02 6:25:55 PM
Type: Note
Author: Please check ref 20